




# Detection of SARS-CoV-2 using dielectric modulated TFET-based biosensor

Vandana Devi Wangkheirakpam<sup>1,\*</sup> , Brinda Bhowmick<sup>1</sup>, and Puspa Devi Pukhrambam<sup>1</sup>

<sup>1</sup>Department of Electronics and Communication, National Institute of Technology Silchar, Silchar, Assam, India

**Received:** 12 November 2021

**Accepted:** 28 February 2022

**Published online:**

16 March 2022

© The Author(s), under exclusive licence to Springer Science+Business Media, LLC, part of Springer Nature 2022

## ABSTRACT

Attributable to the rapid increase in human infection of Coronavirus disease 2019 (COVID-19) caused by severe acute respiratory syndrome coronavirus-2 (SARS-CoV-2), the World Health Organization (WHO) has declared this disease outbreak as a pandemic. This outbreak can be tackled to some extent through proper management and early diagnosis. This work reports a biosensor based on vertical tunnel field-effect transistor (VTFET) developed for the detection of SARS-CoV-2 from the clinical samples through the analysis of its spike, envelope, and DNA proteins. Investigation of the sensitivity of the proposed sensor has been done by calculating the shift in drain current. The dielectric constant equivalent of the virus proteins is used to represent the hybridized biomolecules within the nanogaps. The sensitivity of this proposed sensor is found to be significantly high (order of  $10^6$ ) showing the viability of the device to be a superior sensor. Furthermore, the sensitivity analysis concerning DNA charge density is also performed. The effect of DNA charge density variation on the threshold voltage ( $V_{th}$ ) and sensitivity have also been studied in this work. The proposed sensor is also investigated for its noise performance and observed the sensitivity with and without the effect of interface trap charges. Finally, the proposed sensor is benchmarked against the sensitivity of various FET-based biosensors already published earlier.

## 1 Introduction

The unprecedented outbreak of the novel coronavirus, which is termed as “Coronavirus Disease-2019 (COVID-19)” by the World Health Organization (WHO), has laid hold of the entire world in a great dilemma, forcing lockdown and straining public health care systems. This led to the precarious

positions of numerous governments around the globe facing economic recession. COVID-19 is a respiratory disease caused by a contagious virus known as the severe acute respiratory syndrome coronavirus-2 (SARS-CoV-2) [1]. It is a member of coronaviridae family, a single-stranded positive-sense RNA virus. Similar to the influenza virus, it also blitzed the human respiratory system giving rise to minor

Address correspondence to E-mail: vannawang46@gmail.com

ailments like cough, fever, fatigue, and breathlessness in serious case [2]. Although the exact source of this virus is not known to us, scientists have discovered that its gene sources are typically derived from bats and rodents, and found it to be a member of the  $\beta$ -CoV genera of the coronavirus family. This  $\beta$ -CoV is familiar to the world since there were already two different zoonotic disease outbreaks happened before [4], i.e., SARS-CoV (2002–2003) and MERS-CoV (2012). The COVID-19 was first reported in Wuhan, China's Hubei province in December 2019. Since then, the disease has spread globally like a wildfire due to human-to-human transmission and on January 30, 2020 [3], WHO (World Health Organization) declared it to be a Public Health Emergency of International Concern (PHEIC) [5]. The lifestyles of people all over the world have changed attributable to the outbreak of coronavirus-2019. To control this transmission to some extent, many governments were forced to undertake countrywide lockdowns, recommend to maintain social distancing and self-isolation, and also advice to work from home. Mass testing of the population at large were conducted [6]. Many countries are struggling to produce an efficient vaccine/treatment for this virus. Early diagnosis and management are one of the important means to contain the spread of this contagious virus [7]. The understanding of the structural information along with the pathological information of COVID-19 are required to design various diagnostic methods. The image of this virus was displayed by the Centers for Disease Control and Prevention (CDC), USA [8], and it is round shaped consisting of a thin membrane where envelope and spike proteins are attached as shown in Fig. 1. Its genetic material is RNA rather than a DNA and is covered by the Nucleocapsid proteins (N-Protein). The envelope and spike proteins are termed as E-Protein and S-Protein, respectively [9]. It is also essential to understand the mechanism of the virus involved in recognizing the receptor. COVID-19 causative virus SARS-CoV-2 recognizes the receptor named angiotensin-converting enzyme 2 (ACE2) present in humans. The virus-surface spike protein acts as a mediator for the arrival of coronavirus into host cells. This spike protein consists of receptor-binding domain (RBD) which specifically accepts ACE2 as its receptor. From their crystal structures, it is determined that SARS-CoV RBDs have two parts—a core and a receptor-binding motif (RBM). The RBM

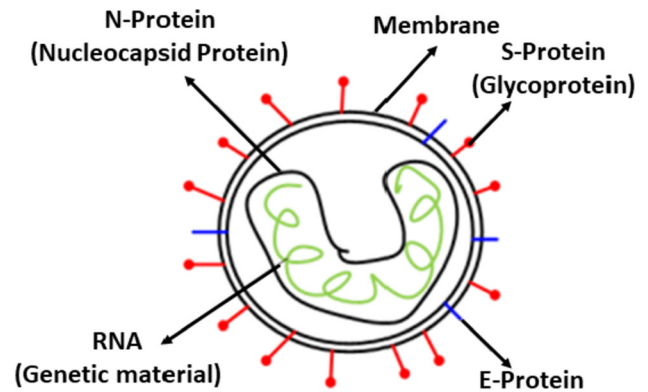


**Fig. 1** Structure of SARS-CoV-2

conciliates the interactions with ACE2. The ACE2 surface also possesses two hotspots for binding SARS-CoV virus [10, 11]. Jian Shang et al. determined the structural basis of receptor recognition by SARS-CoV-2 through crystallization of SARS-CoV-2 RBD–ACE2 complex [12].

The methodologies adopted for detecting SARS-CoV-2 in human at present are real-time reverse transcription-polymerase chain reaction (RT-PCR) and Enzyme-Linked Immunosorbent Assays (ELISA) IgG antibody test. In ELISA test, the related antibodies from the blood serum of patient's body are detected rather than the actual virus [13, 14]. Currently, the primary method for diagnosis is the real-time RT-PCR where the specimen from interior nasal swab is taken to detect the gene of E-protein, RNA (N-Protein) along with open frame reading b1 (OFRb1) and OFRb2. The detection process starts by placing the sample or virus RNA in the testing kit. Next, a replica of this virus RNA is produced by depositing primer over it. Further, this virus RNA is converted to complementary DNA (c-DNA) through reverse transcriptase process and by using DNA polymerization technique, various copies are formed [15]. c-DNA is the synthetic DNA in which the sequence of bases is complementary to that of a given example of DNA. RNA serves as a template for c-DNA synthesis. The final step is to denature and break the DNA into two strands by heating. After this, the primer and reporter molecules which are fluorescent in nature and quencher, collectively known as probe, are added to the denatured DNA helix using annealing processes. The *Thermus Aquaticus* (TAQ) enzyme removes the reporter from the probe. As the reporter gets detached from the quencher, it produces light. In this way, the rRT-PCR

kit detects SARS-CoV-2 [16]. Molecular diagnosis using this technique takes at least 3 h which includes the virus RNA preparation. Furthermore, the diagnostic accuracy can also be affected by these RNA preparation steps. Nowadays, the rapid antigen test (RAT) is also performed where viral antigen is detected. However, since this kind of detection process is also based on label sensor, it is also less accurate. Therefore, highly sensitive diagnostic techniques whose detection processes directly depend on viral antigens in the clinical samples are required for an accurate and rapid detection of COVID-19 [17, 18]. Of all the currently available diagnostic methods, the FET-based biosensors can be a promising candidate with various advantages such as high sensitivity providing instantaneous measurements with a very less quantities of analytes [19, 20]. Such biosensors have great potential in clinical diagnosis, point-of-care testing, and on-site detection. Tunnel field effect transistor (TFET)-based biosensors have the ability to give higher sensitivity and better performance with faster response [21–25]. This transistor is a gated reverse bias p-i-n diode and it works on the principle of band-to-band tunneling giving sub-threshold swing (SS) steeper than that of MOSFET [26–28].

In this work, TFET-based biosensor is studied for diagnosing SARS-CoV-2 through the investigation of electrical property (dielectric constant) of C-DNA and S-protein of the virus. The S-protein of COVID-19 is composed of glycoproteins like biotin-streptavidin and folded proteins whose general dielectric constant approximately ranges from 1 to 4. As per the literature [29, 30], the dielectric constant of DNA lies between 1 and 64. Hence, two ways of virus detection methods are adopted and these are the detection using S-protein and the DNA detection where the virus RNA is converted into its C-DNA. Sensitivities of the proposed TFET-based biosensor are analyzed for both the detection methods. Several FET-based biosensors have been reported in the literature for sensing SARS-CoV-2 [31–34]. However, the proposed biosensor in our work is based on the Tunnel FET which works on the principle of quantum mechanical tunneling and it is well known for its steeper sub-threshold swing characteristics providing faster switching. This peculiar property of TFET is responsible for the impressively high sensitivity when being used in the sensing applications. Also, the sensing process is done by immobilizing the target molecules inside the nanogaps which is created by etching some

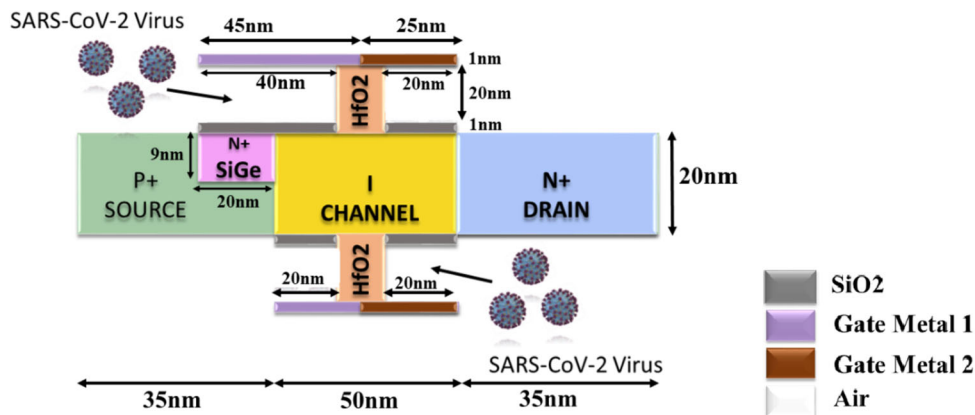
part of the oxide layer. Two types of metal are used for gate. This can avoid the chances of alteration of the chemical properties of the target molecules due to the reaction with the solution of ionic liquid gate.

## 2 Device structure and simulation strategy

Figure 2 shows the 2D schematic of Vertical TFET (VTFET)-based label-free biosensor designed for sensing SARS-CoV-2. It consists of a SiGe pocket with 30% Ge concentration allowing both vertical and lateral tunneling of the device. This N<sup>+</sup> pocket has a doping concentration of  $1 \times 10^{19} \text{ cm}^{-3}$  throughout these analyses. The dimensions of the device are indicated in Fig. 2. Two metal gates,  $\Phi_{m1} = 3.8 \text{ eV}$  (source side) and  $\Phi_{m1} = 5.1 \text{ eV}$  (drain side), are utilized in this sensor design to obtain better  $I_{ON}/I_{OFF}$  ratio. The doping concentration of source, channel, and drain regions are, respectively,  $5 \times 10^{19} \text{ cm}^{-3}$ ,  $1 \times 10^{15} \text{ cm}^{-3}$ , and  $1 \times 10^{18} \text{ cm}^{-3}$ . The fixed dielectric material (HfO<sub>2</sub>) is 10 nm long. A layer of SiO<sub>2</sub> having 1 nm thickness is embedded in the structure to account for the immobilization of receptor molecules as well as for minimization of the leakage current. The entire sensing process is assumed to occur in a dry environment.

All the simulations are done using 2D Sentaurus TCAD tool [35]. The band-to-band tunneling (BTBT) mechanism occurring within the device is executed using non-local BTBT model. The forbidden energy bandgap narrowing due to the higher doping level in the drain and source regions is accounted in the simulation process by the bandgap narrowing model. Shockley Read Hall (SRH) model is included to handle the recombination mechanisms due to indirect bandgap materials. The working principle of this type of biosensor depends on the gate and channel coupling. This coupling is less when the cavities are empty and it increases when the biomolecules are incubated inside the cavities as in this case effective gate capacitance increases. Consequently, the concentration of electron in the channel rises significantly giving higher drain current. In order to carry out this action in the simulation process, the biomolecule to be detected is replaced by an insulator with same value of dielectric constant. Thus, the nanogaps are occupied by this insulator. The condition when the cavities are empty is represented by an insulator

**Fig. 2** 2D cross-sectional view of Vertical TFET-based SARS-CoV-2 sensor



having  $k = 1$  (air). The fabrication aspects are not much focused in this work. However, such type of FET-based dielectric modulated label-free biosensors are successfully fabricated in other reported works. Giwan Seo et al. fabricated an FET-based biosensor for the detection of COVID-19 causative virus in human nasopharyngeal swab specimens where they used SARS-CoV-2 spike antibody for the hybridization process [17]. The detection process of the proposed vertical TFET-based COVID-19 sensor is given in Fig. 3.

### 3 Results and discussion

The fundamental characteristics of the proposed sensor concerning the S-protein and C-DNA are investigated in this section for better understanding of its operation and physics. Although the exact value of dielectric constant of this virus is not declared till now, it is known to us that the dielectric of S-protein ranges from 1 to 4, while the dielectric constant of DNA lies constant between 1 and 64. Therefore, in this work,  $k = 4, 10,$  and  $12$  are used to represent S-protein and C-DNA.

#### 3.1 Sensitivity analysis concerning neutral charge

Figure 4 investigates the  $I_D$ - $V_{GS}$  characteristics of the VTFET-based sensor for various value of dielectric constants ( $k$ ) of the virus protein and C-DNA assuming that they are neutral charged. The amount of drain current rises when the nanogaps are filled with biomolecules ( $k = 4, 10, 12$ ) and its value is less in the empty state of the nanogaps. This is because the hybridization of the biomolecules due to the

immobilized receptors inside the nanogaps imparts a measurable change in the channel conductivity as the effective gate capacitance increases.

$$C_{eff} = \frac{\epsilon_{bio}\epsilon_{SiO_2}}{\epsilon_{bio}t_{SiO_2} + \epsilon_{SiO_2}t_{bio}}, \quad (1)$$

where  $C_{eff}$  is the effective capacitance per unit area assuming that the filled factor of nanogaps is 100%. It is understood from Eq. (1) that  $C_{eff}$  increases with  $\epsilon_{bio}$  (value of  $k$ ). This increases the electric field lines in the channel region and causes the accumulation of more charges. Consequently, the drain current enhances. The corresponding energy band diagrams in both lateral and vertical directions for different values of  $k$  representing the biomolecules are, respectively, plotted in Fig. 5a and b. Band bending is more at  $k = 12$  which explains the higher drain current characteristics in comparison with other  $k$  under consideration. The drain current sensitivity of the proposed SARS-CoV-2 sensor is measured with respect to  $k = 1$  (air), i.e., the state when the nanogaps are empty. The sensitivity is measured using Eq. (2).

$$Sensitivity, S_n = \frac{I_{D,k}}{I_{D,Air(k=1)}} \Big|_{V_{GS}, V_{DS}}, \quad (2)$$

where  $I_{D,k}$  and  $I_{D,Air(k=1)}$ , respectively, indicates the drain current at a fixed gate ( $V_{GS}$ ) and drain voltage ( $V_{DS}$ ) for filled nanogaps (S-proteins or C-DNA) and empty nanogaps. Figure 6a depicts the plot for calculated drain current sensitivity for the three different neutral charged biomolecules under consideration. The sensitivity is found to be in the order of  $10^6$  at  $k = 12$ , which is quite high as compared to the existing devices because of the presence of the SiGe n+ pocket at the source-channel junction. This shows the viability of this biosensor as a



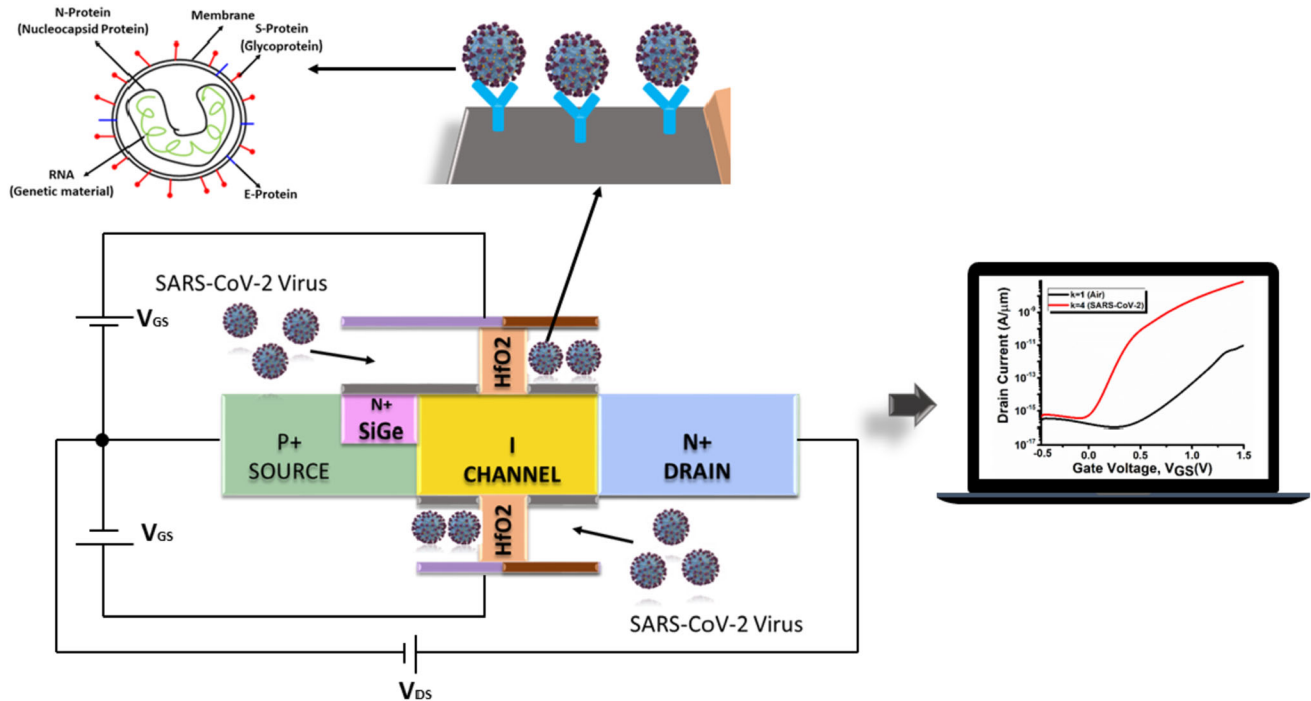


Fig. 3 Operation procedure of vertical TFET-based COVID-19 sensor

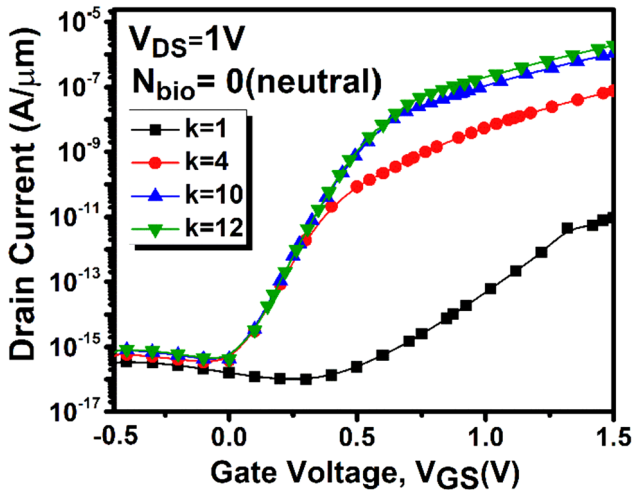


Fig. 4 Transfer characteristics of Vertical TFET-based label-free biosensor for sensing SARS-CoV-2

superior one. The response time of the proposed biosensor is specified as time to rise to 90% of final value, measured from onset of step input change in the measured variable. From Fig. 6b, the response time is found to be  $t_{pLH} = 12$  ps which is very less. This is due to the steeper sub-threshold swing characteristics of TFET. Furthermore,  $I_D-V_{GS}$  characteristics shown in Fig. 4 clearly display the variation in certain DC characteristics like  $I_{ON}$ ,  $V_{th}$ , SS, and  $I_{ON}/$

$I_{OFF}$  for the virus protein and DNA within the nanogaps. The variation of SS and  $I_{ON}/I_{OFF}$  at various value of  $k$  representing S-protein and C-DNA is depicted in Fig. 7. The rise in  $I_{ON}/I_{OFF}$  is about 30% and SS drops by a factor of 1% when the value of  $k$  under consideration increases.

### 3.2 Sensitivity analysis concerning DNA charge density

The method of virus detection using its DNA is done by converting the RNA of the virus into DNA using reverse transcriptase process. The DNA molecules can possess charges and hence it can alter the sensitivity of the sensor depending on the density of the charges. In this section, the responses of the proposed sensor to the positively and negatively charge DNA which are immobilized within the nanogaps are studied. Figure 8a shows the difference in drain current from maximum negative to maximum positive charge density of DNA considered in the simulation. The transfer characteristics is plotted assuming that the nanogaps are fully filled with DNA molecule having  $k = 10$ . To visualize the difference in current characteristics with charge density more clearly, the transfer characteristics is plotted in linear scale in Fig. 8b. The ON-state current and threshold

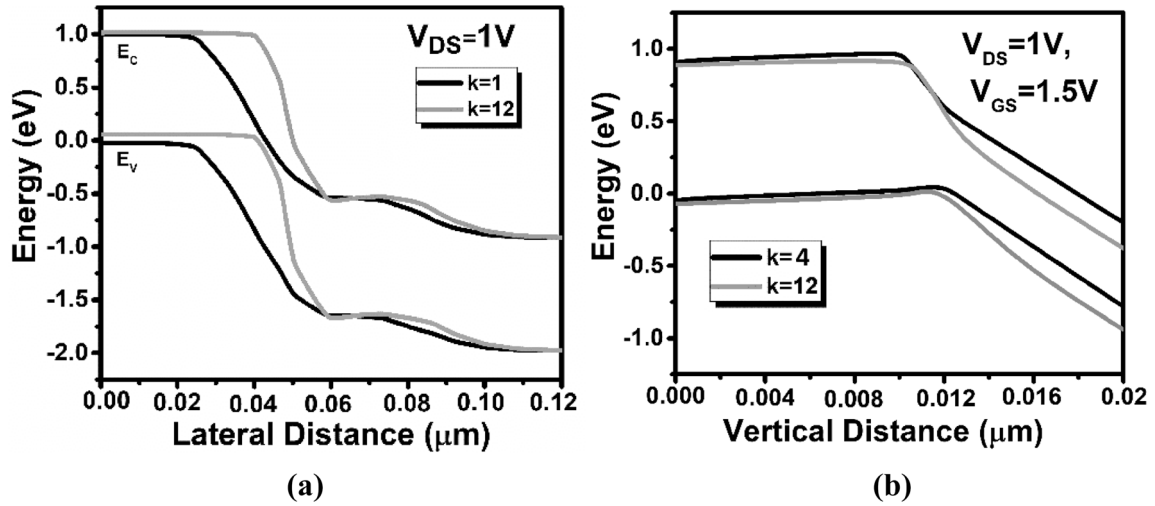


Fig. 5 Conduction and valence band energy distribution over a lateral direction and b vertical direction at various value of k

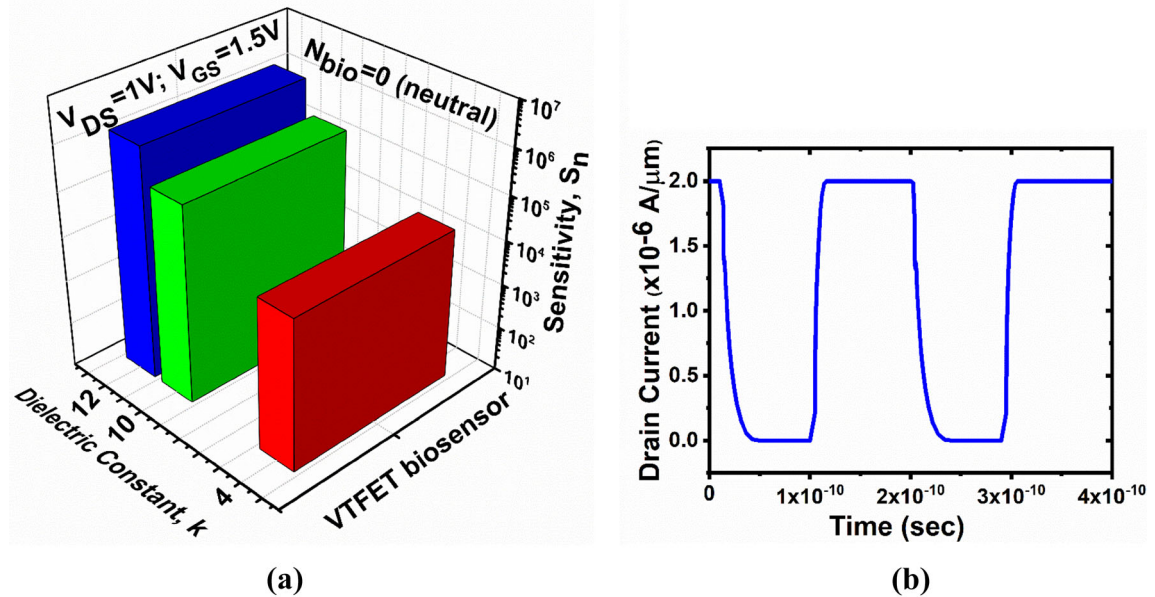


Fig. 6 a Drain current sensitivity of VTFET-based biosensor for neutral charged biomolecules. b Time-dependent response of the VTFET-based biosensor at dielectric constant,  $k = 12$

voltage in both the cases depend on the charge density of the DNA under test. Drain current increases as the positive charge density enhances while it is observed to be declining as the density of negatively charged analytes rises. The threshold voltage ( $V_{th}$ ) is also observed to be declining from maximum value of negative to maximum value of positive charges of the DNA molecules under consideration. Therefore, another method of determining sensitivity is in terms of  $V_{th}$  as it is a function of dielectric constant and charge of the analytes at the interface.

$$Sensitivity, S_n = V_{th,k=1} - V_{th,k}, \tag{3}$$

where  $V_{th,k=1}$  and  $V_{th,k}$  are the  $V_{th}$  of the  $I_D-V_{GS}$  characteristics for empty nanogaps and filled nanogaps, respectively.

The  $I_D-V_{GS}$  characteristics of the proposed sensor at  $k = 1, 4, 10,$  and  $12$  having fixed negative charge density,  $N_{bio} = -1 \times 10^{12} \text{ C/cm}^2$  are plotted in Fig. 9a. The drain current is observed to be shifted towards the right when the density of the negatively charged DNA molecules rises from neutral to  $-2 \times 10^{12} \text{ C/cm}^2$ . The change in  $V_{th}$  is plotted in

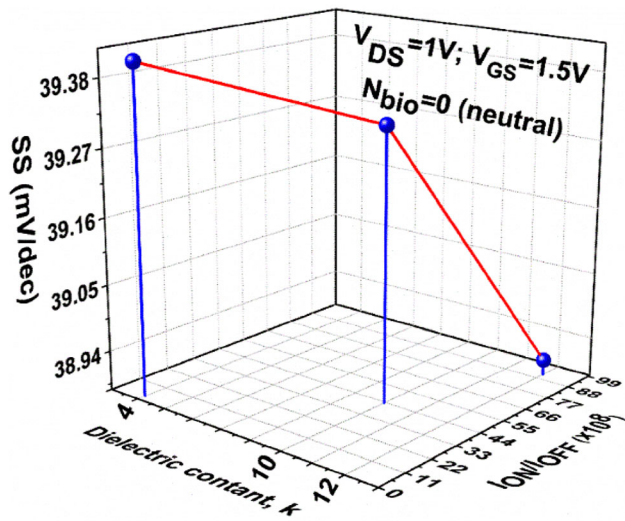


Fig. 7 Variation of sub-threshold swing (SS) and  $I_{ON}/I_{OFF}$  at various value of  $k$  representing S-protein and C-DNA

Fig. 9b for various values of  $k$  considered in this analysis. But, for a particular density of charged DNA,  $V_{th}$  reduces with the increase in  $k$ . Equation 2 is used to calculate the drain current sensitivity. From Fig. 9c, it is clear that the sensitivity declines for the improved values of the negative charge densities of the DNA molecules. This can be explained using the potential balanced equation given in Eq. 4.

$$V_{GS} = \Psi_S + \Phi_{MS} - \left( \frac{q(\mp N)}{C_{eff}} \right), \quad (4)$$

where  $\Psi_S$  represents the surface potential,  $\Phi_{MS}$  is the contact potential,  $q$  gives the unit charge,  $\mp N$  is the biomolecules' charge per unit area ( $N_{bio}$ ), and  $C_{eff}$  is the effective capacitance per unit area. In Eq. (4), for fixed values of  $V_{GS}$  and  $k$ , the increase in the value of  $-N$  will reduce  $\Psi_S$ . The reduction in  $\Psi_S$  is the

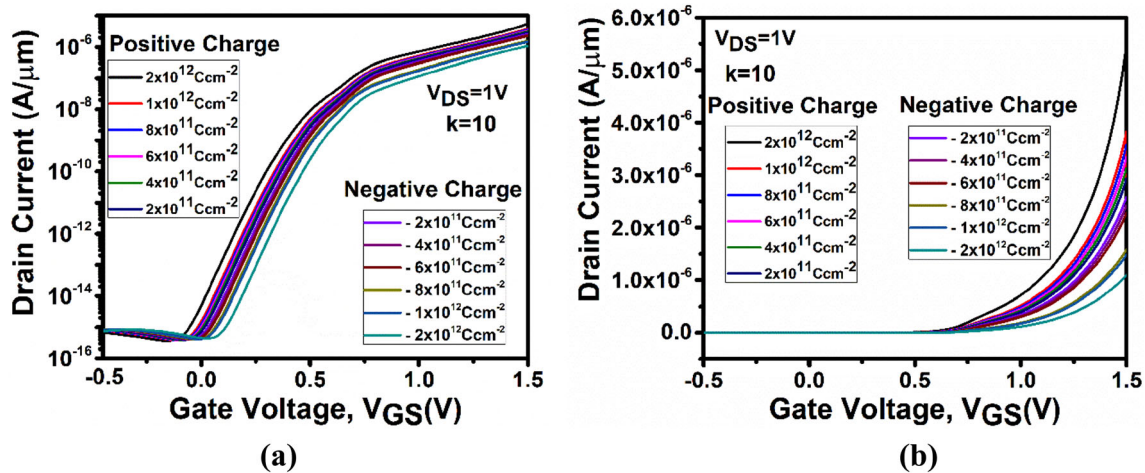


Fig. 8 Variation of transfer characteristics at different DNA charge density where drain current is in a log scale and b linear scale

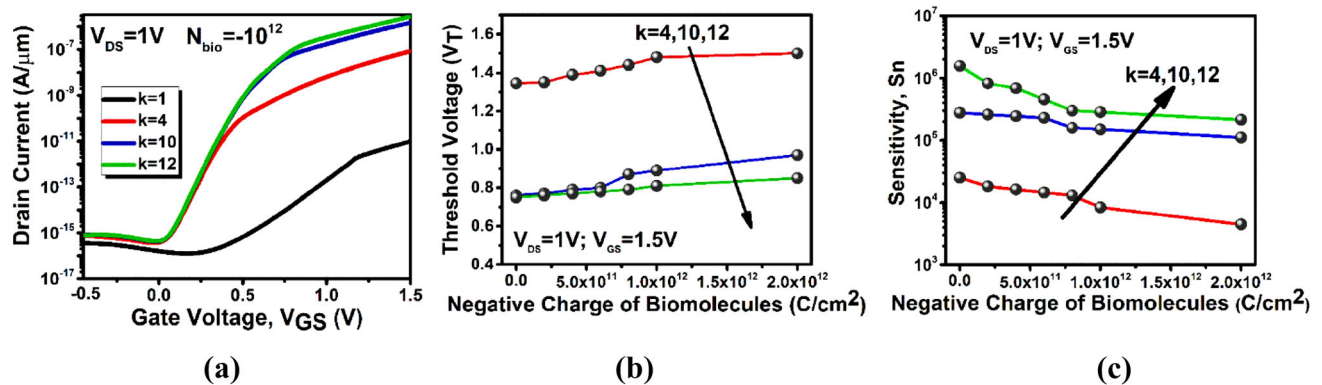


Fig. 9 a Transfer characteristic of VTFET sensor for the detection of SARS-CoV-2 when the DNA charge density is  $-1 \times 10^{12}$   $C/cm^2$ . b Threshold voltage ( $V_T$ ) versus various negative charge

densities of DNA. c Sensitivity ( $S_n$ ) versus various negative charge densities of DNA



reason behind the degradation of drain current and ultimately a reason for the sensitivity reduction. Additionally, at constant  $V_{GS}$  and  $-N$ , the rise in  $k$  value results in the improvement of  $\Psi_S$  which enhances the drain current and thus sensitivity. This explains the improvement of  $S_n$  with the increase in  $k$  value. Again, the term  $-qN/C_{eff}$  in Eq. (4) takes into account the impact of negatively charge biomolecules. The depletion of the channel is limited by this term. Therefore, a higher gate voltage (greater than the case of neutral charged biomolecules) is needed to deplete the channel and hence,  $V_{th}$  rises (Fig. 9b).

Similarly, the impacts of positively charged DNA on the characteristics of the sensor are studied in Fig. 10. Figure 10a shows the  $I_D$ - $V_{GS}$  characteristics of the proposed sensor at  $k = 4, 10$ , and  $12$  considering the effect of positive charges keeping  $N_{bio} = 1 \times 10^{12} \text{ C/cm}^2$ . Reduction of  $V_{th}$  with the increase in the density of the positive charge is observed in Fig. 10b. This is because, the increase in positive charge density ( $+N$ ) in the term  $qN/C_{eff}$  of Eq. (4) leads to the rise in surface potential ( $\Psi_S$ ) at a given  $V_{GS}$ . Thus, the channel conductance of the sensor increases. Likewise, the increase in density of positive charges of DNA improves the sensitivity of the device which can be seen from Fig. 10c.

### 3.3 Effect of scaling on noise in TFET-based biosensor

A semiconductor device faces reliability problems due to the inherent defects like interface trap charges (ITCs) present in the device physics [36]. Hence, the models that explicitly take into account the

occupation and the charge stored on traps must be considered in the simulation. Acceptor-type traps at the interfaces are examined in this section. This type of traps does not possess any charge when it is not occupied and carry the charge of an electron when fully occupied.

Uniform and Gaussian type of distribution are investigated in this work [37].

$$\text{Uniform : } N_0; \text{ for } E_0 - 0.5E_S < E < E_0 + 0.5E_S$$

$$\text{Gaussian : } N_0 \exp\left(-\frac{(E - E_0)^2}{2E_S^2}\right)$$

Here,  $N_0$  is set with the concentration of traps ( $1 \times 10^{13} \text{ eV}^{-1} \text{ cm}^{-2}$ ),  $E_0$  (0 eV) and  $E_S$  (0.1 eV) are given in eV by EnergyMid and EnergySig. The trap charge density distributions against energy are plotted in Fig. 11a. Figure 11b depicts the transfer characteristics curves of VTFET biosensor at  $k = 12$  showing the effect of ITCs. The traps located near the tunneling junction are mainly responsible for the degradation of drain current. They are plotted in Fig. 11a. Figure 11b depicts the transfer characteristics curves of VTFET biosensor at  $k = 12$  showing the effect of ITCs. The traps located near the tunneling junction are mainly responsible for the degradation of drain current. The process of random trapping and detrapping are also one of the major reasons of the fluctuation in the total number of carriers available for current transport [38]. The trapped charges can instigate fluctuation in carrier mobility and electric field too. The noise produced by such traps are studied. This type of noise cannot be completely eliminated since it is inherited in the device physics. Therefore, it has to be minimized by clever choice of

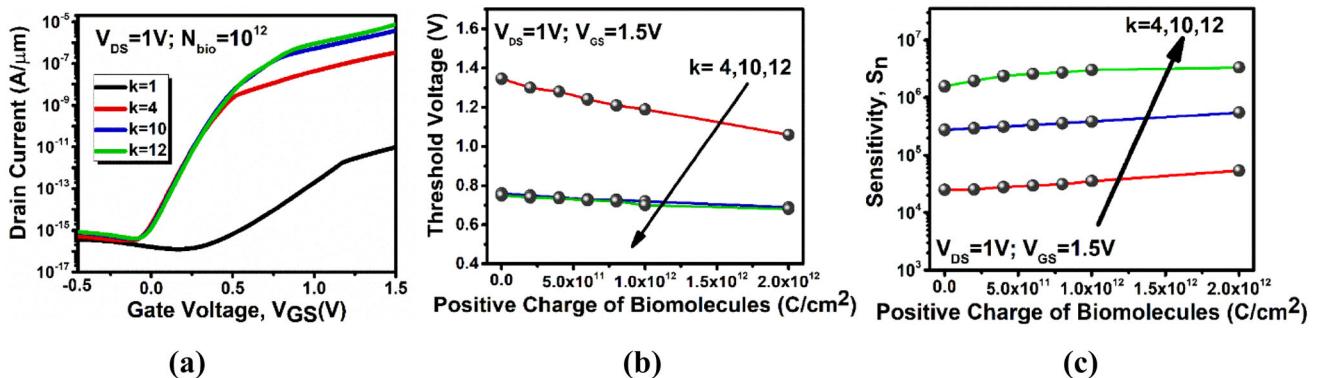


**Fig. 10** a Transfer characteristic of VTFET sensor for the detection of SARS-CoV-2 when the DNA charge density is  $1 \times 10^{12} \text{ C/cm}^2$ . b Threshold voltage ( $V_T$ ) versus various positive

charge densities of DNA. c Sensitivity ( $S_n$ ) versus various positive charge densities of DNA



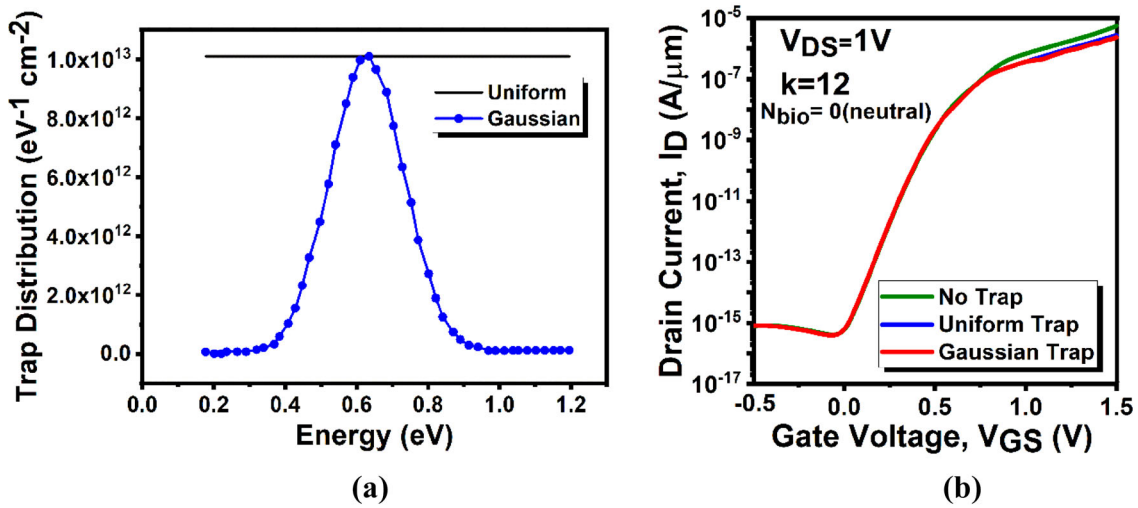


**Fig. 11** a Distribution of trap charges over energy b Influence of uniform and Gaussian type of trap distributions on drain current characteristics

device material and geometry. Effect of pocket length scaling on drain current noise spectral density ( $S_{id}$ ) is shown in Fig. 12a and b for  $f = 1$  MHz and 10 GHz, respectively. Furthermore, the distribution of net  $S_{id}$  over frequency is plotted in Fig. 13. The  $S_{id}$  is higher at lower frequency and its value diminishes for elevated frequency. Hence, this type of noise is known as the low-frequency noise. Net  $S_{id}$  is observed to be higher at  $L_{Pocket} = 10$  nm as compared to 15 nm and 20 nm. Hence, considering the noise as well as drain current aspect,  $L_{Pocket} = 20$  nm is considered for all the analyses. Figure 14 shows the sensitivity variations with and without traps at  $k = 12$ . The sensitivity slightly decreases in the presence of traps but it is high enough to surpass the sensitivity of the state-of-

the-art biosensors. The lower limit of detection (LOD) is measured by considering the signal-to-noise ratio (SNR) extracted from a combination of noise and I-V characterization. The SNR for bioFET devices in terms of number fluctuation model is presented as [39]

$$SNR = \frac{g_m}{\sqrt{S_{id}}} = \frac{1}{\sqrt{S_{VFB}}} = \sqrt{\frac{WLC_{ox}^2 f}{\lambda k T q^2 N_T}} \tag{5}$$

where  $W$  and  $L$  are the widths and lengths of the device, respectively.  $\lambda$  is the tunneling parameter for electrons in silicon oxide,  $k$  is the Boltzmann constant,  $T$  is the temperature,  $f$  is the frequency at which the power of the noise density ( $S_{id}$ ) is measured, and

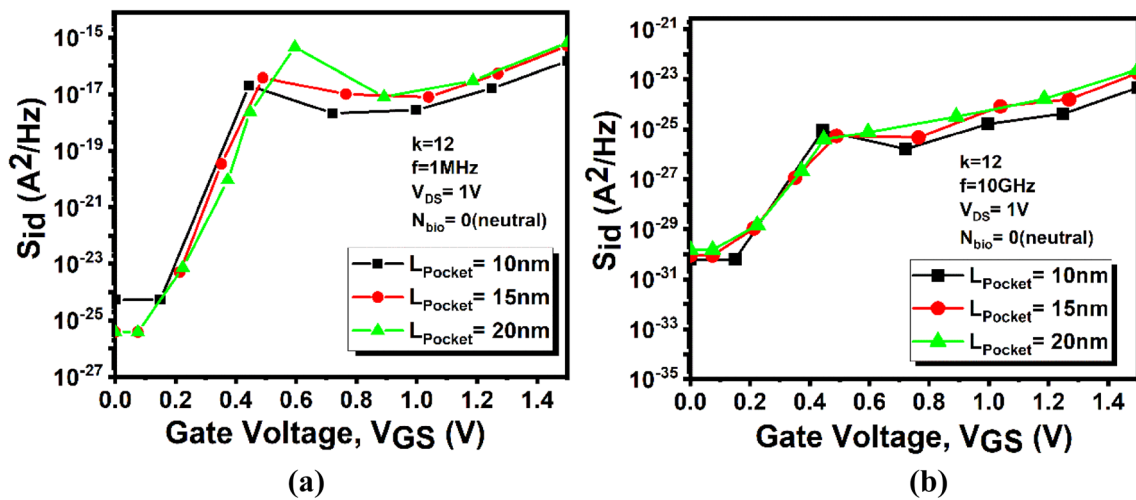


**Fig. 12** Drain current noise spectral density of TFET-based biosensor at a  $f = 1$  MHz b  $f = 10$  GHz

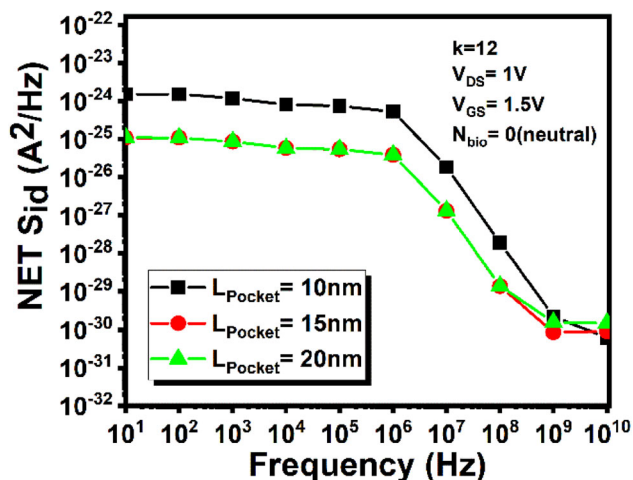


Fig. 13 Net  $S_{id}$  with respect to frequency

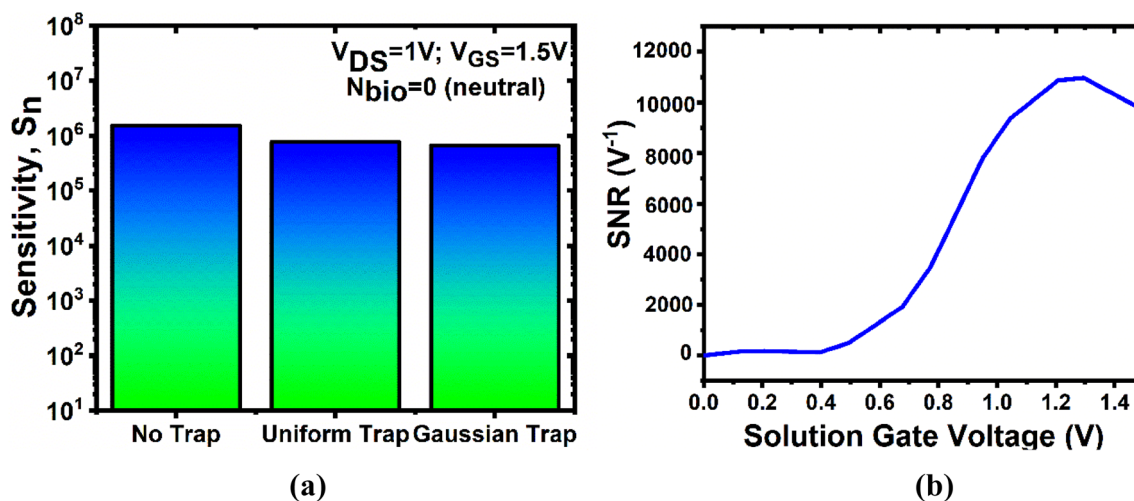


Fig. 14 **a** Sensitivity of VTFET-based biosensor in the presence and absence of traps at  $k = 12$ . **b** Plot of SNR as a function of solution gate voltage

Table 1 Status map of fet-based biosensors

Sl. No	Biosensors	Approx. sensitivity	Response time	Limit of detection
1	Dual metal extended gate TFET sensor for detecting SARS-CoV-2 ( $k = 2, 1$ , $N_{bio} = 1 \times 10^{12} \text{ C/cm}^2$ , $V_{GS} = 0.6 \text{ V}$ ) [17]	$4 \times 10^2$	–	–
2	Direct SARS-CoV-2 Nucleic Acid Detection by Y-Shaped DNA Dual-Probe Transistor Assay, Journal of the American Chemical Society ( $1000 \mu\text{L}^{-1}$ ) [31]	450	0.7 min	0.03 copy/ $\mu\text{L}$ ( $5.01 \times 10^{-20} \text{ M}$ )
3	Two-Dimensional-Material-Based Field-Effect Transistor Biosensor for Detecting COVID-19 Virus (SARS-CoV-2) [32]	$> 1$	$> 120 \text{ min}$	25 fg/ $\mu\text{L}$
4	Graphene Field-Effect Transistor Sensing of Influenza Virus and SARS-CoV-2, ACS Omega [33]	$< 0.5$	50 ms	1 fg/mL
5	Rapid Detection of SARS-CoV-2 Antigens Using High-Purity Semiconducting Single-Walled Carbon Nanotube-Based Field-Effect Transistors [34]	–	2 min	0.55 fg/mL for SAg
6	Dual metal gate SiGe pocket Vertical TFET for detecting SARS-CoV-2 ( $k = 12$ , $N_{bio} = 2 \times 10^{12} \text{ C/cm}^2$ , $V_{GS} = 1.5 \text{ V}$ ) [ This work ]	$2 \times 10^6$	12psec	$\sim 89 \mu\text{V}$

$C_{ox}$  is the oxide capacitance per unit area.  $N_T$  is the trap density including surface states and interface traps/defects. The LOD follows the minimum detectable surface potential change and it is given by  $1/\text{SNR}$ , which is limited by the flat-band voltage fluctuations due to the effects of traps and interface states [39, 40]. Figure 14b shows the plot of SNR as a function of solution gate voltage. The peak SNR value of 11,200 is obtained which translates to a minimum detectable voltage of  $\sim 89 \mu\text{V}$ . SNR is maximum at the point of peak transconductance ( $g_m$ ). Hence, the LOD is significantly low for this very less minimum detectable voltage.

### 3.4 Benchmarking against various reported work

The proposed VTFET-based biosensor for the detection of SARS-CoV-2 is benchmarked in this section against the parameters such as sensitivities, response time and limit of detection of various simulated, analytically modeled, and fabricated works published till date. Table 1 shows the status map of various FET-based sensors. The term ‘approximate sensitivity’ is used in Table 1 as they are extracted from the published work.

## 4 Conclusion

Developing a highly sensitive and rapid biosensor for the detection of SARS-CoV-2 has become extremely important to contain the COVID-19 pandemic to some extent. In this work, a vertical TFET-based dielectric modulated biosensor for sensing COVID-19 causative virus (SARS-CoV-2) is proposed. The utilization of  $n+$  pocket at the source side provides better drain current of the device. The simulation data clearly remark a very high sensitivity for different dielectric virus proteins (S-protein and DNA) which are hybridized within the nanogaps. An optimum sensitivity of  $1.56 \times 10^6$  is obtained for fully filled neutral biomolecules when  $k = 12$  which is quite high. Further, investigation has been done on the change in sensitivity due to the effect of virus DNA charge density. The sensitivity increases when the nanogaps are filled with positively charged biomolecules while it is observed to be declining when the analytes are negatively charged. The sensitivity of this sensor is also studied in the presence of noises induced by the interface trap charges. Finally, a status map of published FET-based sensors is studied and it reveals the viability of the proposed VTFET-based biosensor to be a superior one with low operating power and better sensitivity.

### Author contributions

All persons who meet authorship criteria are listed as authors, and all authors certify that they have participated sufficiently in the work to take public responsibility for the content, including participation

in the concept, design, analysis, writing, or revision of the manuscript. Each author certifies that this material or similar material has not been and will not be submitted to or published in any other publication. They further confirm that the order of authors listed in the manuscript has been approved by all of them.

### Funding

The authors declare that no funds, grants, or other support were received during the preparation of this manuscript.

### Data availability

There are no data associated with this research work.

### Declarations

**Conflict of interest** The authors declare that they have no competing interests.

**Research involved in human and animal rights** There is no animal involved in this research work.

### References

1. S. Vaudenay, IACR Cryptol. ePrint Arch., **20**, 531 (2020) <https://eprint.iacr.org/2020/531>
2. M. Cascella, M. Rajnik, A. Cuomo, S. C. Dulebohn, R. D. Napoli, StatPearls [Internet]. Treasure Island, FL, USA: StatPearls Publishing (2020) <https://www.ncbi.nlm.nih.gov/books/NBK554776/>
3. World Health Organization. Coronavirus disease (COVID-19) Pandemic. [<https://www.who.int/emergencies/diseases/novel-coronavirus-2019>]
4. V. Chamola, V. Hassija, V. Gupta, M. Guizani, IEEE Access **8**, 90225 (2020). <https://doi.org/10.1109/ACCESS.2020.2992341>
5. N. Ahmed, R.A. Michelin, W. Xue, S. Ruj, R. Malaney, S.S. Kanhere, A. Seneviratne, W. Hu, H. Janicke, S.K. Jha, IEEE Access **8**, 1345 (2020). <https://doi.org/10.1109/ACCESS.2020.3010226>
6. C. Drosten et al., N. Engl. J. Med. **348**, 1967 (2003)
7. M. Zaki, S. van Boheemen, T.M. Bestebroer, A.D. Osterhaus, R.A. Fouchier, Isolation of a novel coronavirus from a man with Pneumonia in Saudi Arabia. N. Engl. J. Med. **367**, 1814 (2012)

8. <https://emergency.cdc.gov/recentincidents/>
9. Ou, Xiuyuan, Y. Liu, X. Lei et al., *Nat. Commun.* **11**(1620), 1–12 (2020). <https://doi.org/10.1038/s41467-020-15562-9>
10. F. Li, W. Li, M. Farzan, S.C. Harrison, *Science* (2005). <https://doi.org/10.1126/science.1116480>
11. W. Li et al., *Nature* **426**, 450 (2003)
12. J. Shang et al., *Nature* **581**, 221 (2020). <https://doi.org/10.1038/s41586-020-2179-y>
13. Smart Detect SARS-CoV-2 rRT-PCR Kit Instructions for Use for Emergency Use Authorization (EUA), pp. 1–18, [<https://www.fda.gov/media/136786/download>]
14. XPRSARS-COV2–10 302–3562, Rev B April 2020 Instructions for Use For Use Under an Emergency Use Authorization (EUA), pp. Apr. 2020 [<https://www.fda.gov/media/136314/download>]
15. SARS-CoV-2 RNA, Qualitative Real-Time RT-PCR (Test Code 39433) Package Insert For Emergency Use, pp. 1–18, [<https://www.fda.gov/media/136231/download>]
16. Mount Sinai Laboratory COVID-19 ELISA IgG Antibody Test EUA, pp. 1–6, [<https://www.fda.gov/media/137029/download>]
17. S. Yadav, A. Gedam, S. Tirkey, *IEEE Sens. J.* (2020). <https://doi.org/10.1109/JSEN.2020.3019036>
18. G. Seo et al., *ACS Nano* **14**, 5135 (2020). <https://doi.org/10.1021/acsnano.0c02823>
19. W.V. Devi, B. Bhowmick, *Micro Nano Lett.* **14**, 69 (2019). <https://doi.org/10.1049/mnl.2018.5086>
20. D. Sarkar, K. Banerjee, *Appl. Phys. Lett.* **100**, 143108 (2012)
21. H. Im, X.-J. Huang, B. Gu, Y.-K. Choi, *Nat. Nanotechnol.* **2**, 430 (2007)
22. S. Kanungo, S. Chattopadhyay, P.S. Gupta, H. Rahaman, *IEEE Trans. Electron. Devices* **62**, 994 (2015)
23. R. Narang, M. Saxena, R.S. Gupta, M. Gupta, *IEEE Trans. Nanotechnol.* **14**, 427 (2015)
24. S. Kanungo, S. Chattopadhyay, P.S. Gupta, K. Sinha, H. Rahaman, *IEEE Trans. Electron. Devices* **63**, 2589 (2016)
25. M. Verma, S. Tirkey, S. Yadav, D. Sharma, D.S. Yadav, *IEEE Trans. Electron. Devices* **64**, 3841 (2017)
26. R. Goswami, B. Bhowmick, *IEEE Sens. J.* **19**, 9600 (2019)
27. W.V. Devi, B. Bhowmick, P.D. Pukhrabam, *IEEE Trans. Electron. Devices* **67**, 2133 (2020). <https://doi.org/10.1109/TED.2020.2981303>
28. V.D. Wangkheirakpam, B. Bhowmick, P.D. Pukhrabam, *IEEE Trans. Nanotechnol.* **19**, 156 (2020). <https://doi.org/10.1109/TNANO.2020.2969206>
29. M.K. Gilson, B.H. Honig, *Biopolymers* **25**, 2097 (1986). <https://doi.org/10.1002/bip.360251106>
30. C.H. Kim, C. Jung, H.G. Park, Y.K. Choi, *BioChip J.* **2**, 127 (2008)
31. Derong et al., *J. Am. Chem. Soc.* **143**, 17004–17014 (2021)
32. Fathi-Hafshejani et al., *ACS Nano* **15**, 11461–11469 (2021)
33. Li et al., *ACS Omega* **6**, 6643–6653 (2021)
34. Shao et al., *ACS Appl. Mater. Interfaces.* **13**, 10321–10327 (2021)
35. *Sentaurus Device User*, Synopsys, Mountain View, CA, USA, 2009
36. S.T. Bu, D.M. Huang, G.F. Jiao, H.Y. Yu, Ming-Fu Li (2017) **137**, 95 <https://doi.org/10.1016/j.sse.2017.08.008>.
37. R. Goswami, B. Bhowmick, S. Baishya, *Microelectron. J.* **53**, 16 (2016)
38. V.D. Wangkheirakpam, B. Bhowmick, P.D. Pukhrabam, *Microelectron. J.* **114**, 105124 (2021). <https://doi.org/10.1016/j.mejo.2021.105124>
39. N.K. Rajan, K. Brower, X. Duan, M.A. Reed, *Applied Physics Letter* **104**, 084106–084111 (2014). <https://doi.org/10.1063/1.4867025>
40. N.K. Rajan, D.A. Routenberg, M.A. Reed, *Applied Physics Letter* **98**, 264107–264111 (2011). <https://doi.org/10.1063/1.3608155>

**Publisher's Note** Springer Nature remains neutral with regard to jurisdictional claims in published maps and institutional affiliations.